The Astrophysical Journal, 951:36 (11pp), 2023 July 1 https://doi.org/10.3847/1538-4357/acd75d

Misaligned Jets from Sgr A* and the Origin of Fermi/eROSITA Bubbles

Kartick C. Sarkar[1,2], Santanu Mondal[3], Prateek Sharma[4], and Tsvi Piran[2]
[1] School of Physics and Astronomy, Tel Aviv University, Tel Aviv, Israel; kcsarkar@tauex.tau.ac.il, kartick.c.sarkar100@gmail.com
[2] Racah Institute of Physics, The Hebrew University of Jerusalem, Israel
[3] Indian Institute of Astrophysics, 2nd Block, Koramangala, Bangalore 560034, India
[4] Department of Physics and Joint Astronomy Program, Indian Institute of Science, Bangalore 560012, India
Received 2022 November 23; revised 2023 May 7; accepted 2023 May 18; published 2023 July 3

Abstract

One of the leading explanations for the origin of Fermi Bubbles is past jet activity in the Galactic center supermassive black hole Sgr A*. The claimed jets are often assumed to be perpendicular to the Galactic plane. Motivated by the orientation of pc-scale nuclear stellar disk and gas streams, as well as a low inclination of the accretion disk around Sgr A* inferred by the Event Horizon Telescope, we perform hydrodynamical simulations of nuclear jets significantly tilted relative to the Galactic rotation axis. The observed axisymmetry and hemisymmetry (north–south symmetry) of Fermi/eROSITA bubbles (FEBs) due to quasi-steady jets in Sgr A* could be produced if the jet had a super-Eddington power ($\gtrsim 5\times10^{44}$ erg s^{-1}) for a short time (jet active period $\lesssim$6 kyr) for a reasonable jet opening angle ($\lesssim$10°). Such powerful explosions are, however, incompatible with the observed O VIII/O VII line ratio toward the bubbles, even after considering electron–proton temperature nonequilibrium. We argue that the only remaining options for producing FEBs are (i) a low-luminosity ($\approx10^4$0.5–41 erg s^{-1}) magnetically dominated jet or accretion wind from the Sgr A*, or (ii) a supernovae or tidal disruption event driven wind of a similar luminosity from the Galactic center.

Unified Astronomy Thesaurus concepts: Jets (870); Milky Way Galaxy (1054); Galactic center (565); Circumgalactic medium (1879); Diffuse x-ray background (384); Hydrodynamical simulations (767); Superbubbles (1656)

1. Introduction

The decade-old discovery of two giant gamma-ray bubbles toward the Galactic Center (GC), called the Fermi Bubbles (FBs; Su et al. 2010; Ackermann et al. 2014; Selig et al. 2015), spurred a discussion of their origin. The recent discovery of X-ray structures in the southern Galactic hemisphere by e-Rosita (Predehl et al. 2020), which appear to be the counterparts of the known X-ray features in the northern hemisphere, has reignited the quest for the origin of the Fermi/eROSITA bubbles (FEBs). Leading models are (i) the star formation wind driven scenario where overlapping supernovae and massive stellar winds produce a biconical outflow perpendicular to the Galactic disk (Lacki 2014; Sarkar et al. 2015a; Crocker et al. 2015; Sarkar et al. 2017; Sarkar 2019) and (ii) the central supermassive black hole (SMBH; Mass $M_{\rm bh}\approx4\times10^6\,M_\odot$) wind/jet-driven scenarios where FEBs are powered by accretion onto the SMBH (Guo & Mathews 2012; Zubovas & Nayakshin 2012; Mou et al. 2014; Keshet & Gurwich 2017; Zhang & Guo 2020; Mondal et al. 2022; Yang et al. 2022). These models have varying degrees of success in reproducing the FEBs in different wave bands.

While the scenarios driven by star formation require a star formation rate close to the observations (Nogueras-Lara et al. 2020), the scenarios driven by SMBH jet/wind typically assume an enhanced mechanical power ($\sim10^{-3}$–$10^{-1}L_{\rm Edd}$) of the SMBH in the recent past, because the current mechanical luminosity (power) of Sgr A* is estimated to be 10^{-8}–$10^{-6}\,L_{\rm Edd}$ (Agol 2000; Marrone et al. 2006).

The strongest support for the scenario driven by an SMBH jet is the presence of subparsec nuclear stellar disks, subparsec gaseous streams, and the large-scale ionization cone in the Galaxy (Paumard et al. 2006; Genzel et al. 2010; Bland-Hawthorn et al. 2019), indicating a past accretion event in Sgr A* about a few Myr ago. The possible jet activity from this event could have created FEBs. However, in current jet-driven FB simulations, the jets are injected perpendicular to the Galactic plane (parallel to the Galactic rotation axis), while observations of the subparsec stellar disks/streams find that their rotation vectors are inclined at an angle of 24°–45° from the Galactic rotation axis (see Bartko et al. 2009; Zhao et al. 2009; Genzel et al. 2010; Tsuboi et al. 2018, for a summary of the subparsec structures). Recent Event Horizon Telescope (EHT) mm images of Sgr A* indicate that the accretion disk angular momentum at a few gravitational radii is directed at an angle of $\gtrsim$60° away from the Galactic rotation axis (Akiyama et al. 2022). Additionally, Yusef-Zadeh et al. (2020) find evidence of jet-like structures very close to the Sgr A* that are lying on the Galactic plane. They note that the difference in their claimed jet direction and the nuclear stellar disk (which has an orientation similar to that of EHT) may be due to the temporary angular momentum of the stellar wind that is feeding the BH. It is, therefore, more reasonable to assume that a possible nuclear jet launched by Sgr A* in the past would be significantly misaligned relative to the Galactic rotation axis.

Recently, galaxy formation simulations have been able to resolve gaseous dynamics around an SMBH as the gas is accreted from the kpc scale to the subpc scale. The simulations find that the subpc accretion disk around the SMBH in the AGN phase is tilted by 0°–60° with a time-averaged mean at ~35° with respect to the kpc-scale gaseous disk (Anglés-Alcázar et al. 2021). This means, from a galaxy formation point

of view, MW-type galaxies are not expected to align their subpc accretion disk with the galactic rotation axis. There is, therefore, enough evidence suggesting that a plausible jet from the SMBH is most likely to be directed significantly away from the Galactic rotation axis. Note, however, that it is also claimed that the jet, at least in the past, was very close to the galactic axis (Li et al. 2013; Bland-Hawthorn et al. 2019; Cecil et al. 2021). However, as we show later (see Section 2.3), even if the jet is not inclined, it simply does not manage to deposit the required energy ($\sim 10^{56}$ erg) before it reaches the required $\sim$10 kpc to produce the Fermi/eROSITA Bubbles.

The observable features produced by a jet in our galaxy would largely depend on the interaction of the jet and the ambient medium, i.e., the interstellar and circumgalactic medium (ISM/CGM), and not on just on its original direction. However, if the jet-ambient interaction is strong enough, such that the jet is choked before it emerges from the high-density region of the interstellar and circumgalactic medium, then all the jet kinetic energy is converted into the thermal energy of the expanding cocoon. We call this process "jet dissipation." This happens typically when the jet engine stops before the ejecta emerges from the dense surrounding region, but other possibilities like kink instability of a weak magnetic jet could also lead to dissipation (Tchekhovskoy & Bromberg 2016). For a dissipated jet, the shape of the cocoon will be determined not by the jet direction but by the density gradient of the ambient medium, which is naturally perpendicular to the Galaxy. Because the observed FEBs are axisymmetric (east–west symmetry) and hemisymmetric (north–south symmetry) to a very high degree at the solar vantage point, they must also be intrinsically symmetric. Therefore, given that the expected direction of the jet is not perpendicular to the Galactic disk, it is reasonable to conclude that dissipation is essential to produce the observed FEBs.[5]

The power and the active duration of a jet from the SMBH can vary by many orders of magnitude depending on the available gas and its accretion rate onto the SMBH. Given the observed total energy of the FEB, $E_{\rm FEBs} \approx 10^{56}$ erg (Predehl et al. 2020), the jet duration ($t_{\rm inj}$) and its power (L_j) must satisfy:

$$E_{\rm FEBs} = L_j\ t_{\rm inj}. \quad (1)$$

Thus, more powerful jets should operate for shorter periods.

Several authors have argued that jet dissipation can happen for low-power jets in a highly clumpy medium (Rosen et al. 1999; Mukherjee et al. 2016, 2018, 2020; Tanner & Weaver 2022). However, the physical setup of these simulations is different from ours, i.e., they use a highly clumpy medium. Further, these simulations used a rather low resolution that appears insufficient to resolve jet collimation, and it is possible that the results were influenced by this (see Appendix B for a detailed discussion). In this paper, we show that only high-power jets ($L_j \gtrsim L_{\rm edd}$) that are choked (i.e., without active injection; because $t_{\rm inj} = E_{\rm FEBs}/L_j$) before the cocoon leaves the ISM can be dissipated. However, we argue that such high-power jets are inconsistent with the observed O VIII/O VII line ratio constraints (Miller & Bregman 2016; Sarkar et al. 2017) and therefore are ruled out as the origin of the FEBs.

[5] In quasi-spherical flows, such as the winds driven by star formation or the accretion-driven winds, the energy injection is inherently isotropic and hence the bubble/cocoon follows the ambient density gradient.

This paper is organized as follows. We present the results from our numerical simulations in Section 2, in addition to showing the necessity of jet dissipation within the ISM for producing symmetric FEBs. We provide analytical arguments supporting our simulations as well as discuss general requirements for the dissipation of nonmagnetic jets in Section 3. In Section 4, we discuss possible implications of short-lived and powerful jets with respect to the O VIII/O VII constraint. In Section 5, we consider the fate of magnetic jets, accretion winds, and wind bubbles driven by star formation. Section 6 summarizes our findings on the origin of the FEBs.

2. Hydrodynamical Simulations

2.1. Numerical Setup

We perform 3D hydrodynamical simulations of jets expanding in a realistic ISM/CGM of the Galaxy using the hydrodynamic code PLUTO (Mignone et al. 2007). The simulations are performed in 3D-spherical coordinates with the Galactic disk lying on the $\phi = 0180°$ plane and the rotation axis pointing along the θ, $\phi = 90°$, 90° direction. This special coordinate setup avoids possible numerical artifacts at the $\theta = 0$, π axis (coordinate singularities). Although the jets are supposed to be launched at a subAU scale in Sgr A*, we cannot resolve the launching region while simultaneously modeling $\sim$10 kpc FEBs in the same simulation box. Our fiducial simulation box, therefore, extends radially (i) from 10 pc to 12 kpc with a uniform 2 pc resolution until 300 pc and 360 logarithmic grids outside, (ii) from 5° to 135° in the θ-direction with 0°.5 resolution, and (iii) from 50° to 130° in the ϕ-direction with 0°.45 resolution. We have ensured that this resolution is sufficient to resolve the jet dynamics and produce numerically converged bubbles (see Appendix A for details on the grid structure).

The initial density distribution consists of a rotating ISM disk (central density $=1\ m_{\rm p}\ {\rm cm}^{-3}$ and turbulent velocity of 24 km s^{-1}) and an isothermal CGM (central density $=0.019\ m_{\rm p}$ cm^{-3} and $T = 2 \times 10^6$ K). The initial gaseous distribution is in steady-state equilibrium confined by the background gravity of the dark matter, stellar disk, and the stellar bulge. A detailed description of the setup is given in Sarkar et al. (2015b, 2017). We do not include radiative cooling in the simulations, because the dynamical time of the shock in ISM or CGM is shorter than the cooling time in the medium.

As an example of a tilted jet motivated by observational constraints, the hydrodynamical jet is launched at an angle of 45° from the Galactic pole and has a half opening angle $\theta_0 = 10°$. The jet axis lies in the θ, $\phi = 45°$, 90° direction (see Figure 1 for a cartoon of the geometry). The jets are launched by continuously adding mass and keeping the velocity of the fluid at $v_j = 0.1c$ within the solid angle of the jet and in a region $r \leqslant 30$ pc from the center. The mass addition rate equals the total mass outflow rate ($2L_j/v_j^2$) of the jet.

2.2. Cocoon Dynamics

We perform four simulations with respective jet powers of 2×10^{40} (low-power; LP), 2×10^{41} (medium power; MP), 2×10^{42} (high power; HP), and 2×10^{44} erg s^{-1} (Eddington power; EP), the results for which are shown in Figure 2. Different columns in the figure represent different luminosities. The snapshots are shown at times when the Galactic latitude, b, of the outer edge of the shock reaches $\sim$60°–70° in the

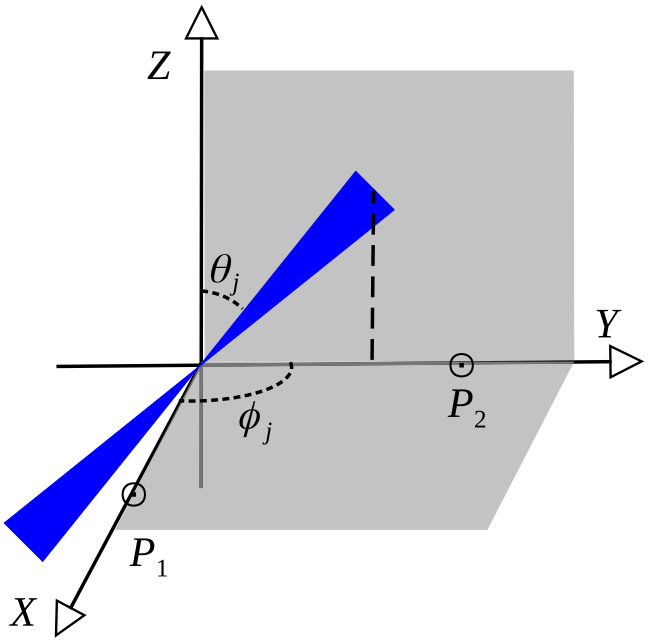

Figure 1. The geometry of the jet in the simulation box and the different points of view for the projection map. In this cartoon, the Galactic disk lies in the X–Y plane and the jet lies in the Y–Z plane. The axis of the jet makes an angle $\theta_j = 45^\circ$ with the Z-axis and $\phi_j = 90^\circ$ with the X-axis. For the in-plane projection map, the observer is at point P_1 (on the X-axis), and the out-of-plane projection represents a view from the point P_2 (on the Y-axis).

northern hemisphere, corresponding to the size of the eROSITA bubbles. The density slices for the LP, MP, and HP cases show that the jet clearly "remembers" its injection direction and it produces cocoons that are significantly tilted from the Galactic pole. Although the LP and MP cocoons are wider than the HP case, they are still significantly tilted, as the jets in these cases have not dissipated. This is in contrast to the results presented by several authors (see Mukherjee et al. 2018; Tanner & Weaver 2022), where the low-power jets show dissipation. Based on several simulations of a comparable resolution and a similar jet-injection method as in those papers, we also find dissipation for low-power jets. We stress that the dissipation seen in these Cartesian box simulations could be due to the inability to numerically resolve the recollimation process at the jet base (see Appendix B) For us, dissipation happens only for the EP jets where the jet engine is turned off and the jet is choked ($t_{\rm inj} \approx 16$ kyr) before it can break out of the ISM (similar to the cocoon dynamics in gamma-ray bursts; Pais et al. 2023). Once choked, the dynamics of the cocoons that form in such a short-duration burst is very similar to that of a Sedov–Taylor blast wave, and therefore it follows the density gradient of the ambient medium (in this case, the ISM/CGM).

2.3. Projection Maps

The tilted cocoons will never produce symmetric FEBs, irrespective of the emission mechanism for γ-rays. This means that the dissipation of the jets and the subsequent vertical rise of the cocoons along the Galactic rotation axis are essential for jet-driven FEBs. Projection effects profoundly affect the observational appearance of FEBs. Given the uncertainty on inclination and the position angle of the claimed jet (Genzel et al. 2010; although recent EHT images of Sgr A* suggest an almost face-on jet pointing toward us), our vantage point will change the appearance of the FEBs. To investigate the influence of such projections, we calculate the soft X-ray (0.5–2.0 keV) surface brightness maps from the local density, temperature, and metallicity ($=0.5\ Z_\odot$) of the gas assuming a MEKAL plasma model (Mewe et al. 1985, 1986; Liedahl et al. 1995). We produce the X-ray surface brightness maps for our simulations from the solar vantage point using the projection software, PASS[6] (Sarkar et al. 2017). The projection maps also consider the effect of an extended hydrostatic CGM until 100 kpc that is not included within the simulation box.

The middle and bottom rows of Figure 2 show the X-ray surface brightness maps projected into the plane of the sky in galactic coordinates using the Aitoff projection method (azimuthal equidistant projection; Snyder 1993).[7] We use two different vantage points with respect to the orientation of the jet: one, perpendicular to the plane of the jet at r, θ, $\phi = 8.5$ kpc, 90°, 0° such that the jets lie on the plane of the sky (in-plane projection; middle panel); and a second, in the plane of the jet at r, θ, $\phi = 8.5$ kpc, 0°, 90° such that the jets lie out of the sky plane (out-of-plane projection: lowest panel), to show the range of possible projection effects (see Figure 1). The tilt in the cocoons is visible in the in-plane projection for all cases, except in EP, for which the tilt is not very apparent, and the cocoon seems to be roughly symmetric.[8] As expected, the out-of-plane view appears axisymmetric for all cases. However, because one of the cocoons now approaches the Sun, it is much closer than its counterpart in the other hemisphere. Therefore, the approaching cocoon appears larger than the receding one, making them non-hemisymmetric, as seen in the lowest panel of Figure 2. It is therefore clear that the tilted jets produce either axisymmetric cocoons or hemisymmetric cocoons but never both together.[9] In contrast, when the jets are dissipated due to early jet choking, the cocoon follows the density gradient, which itself follows the axisymmetric and hemisymmetric gravitational potential of the Galaxy.[10]

Based on the above simulations, we conclude that, if indeed the FEBs were produced by jet activity at the Galactic center and if the jet was significantly tilted from the Galaxy rotation axis, the jet must have a power $L \gtrsim 2 \times 10^{44}$ erg s^{-1} or $\gtrsim L_{\rm Edd}$. However, we note that our simulations only consider fixed (although reasonable) values of the jet velocity and opening angle. The condition for jet dissipation will depend on these parameters, and one needs a large suite of simulations to explore the parameter space, which is beyond the scope of the present paper. Instead, we provide theoretical arguments to understand the process of dissipation in the next section, and obtain general limits on the jet power.

It is important to note that even a low-power jet that was ejected perpendicular to the Galactic disk and that had not dissipated early enough would reach the height of the FEBs (i.e., $\sim$10 kpc) at $\approx$10 Myr (for the LP case) or $\approx$5 Myr (for the MP case), as evident from Figure 2. In such cases, the total injected energy of the cocoon would be $\approx 6 \times 10^{54}$ erg (LP case) or 3×10^{55} (MP case) erg, much less than the energy of

[6] Freely available at https://gitlab.com/kartickchsarkar/PASS-EOV.
[7] https://en.wikipedia.org/wiki/Aitoff_projection
[8] We also performed a simulation for 2×10^{43} erg s^{-1} for which the cocoons show a significant asymmetry around the Galactic plane and the rotation axis.
[9] We do not investigate the upper limit on the jet inclination that can produce axisymmetric and hemisymmtric jets. However, as noted later in this section, a noninclined jet fails to inject enough energy into the FEBs before it reaches the required $\sim$10 kpc.
[10] The slight north–south asymmetry in the EP case may be nullified by a small density asymmetry in the two hemispheres (see Sarkar 2019).

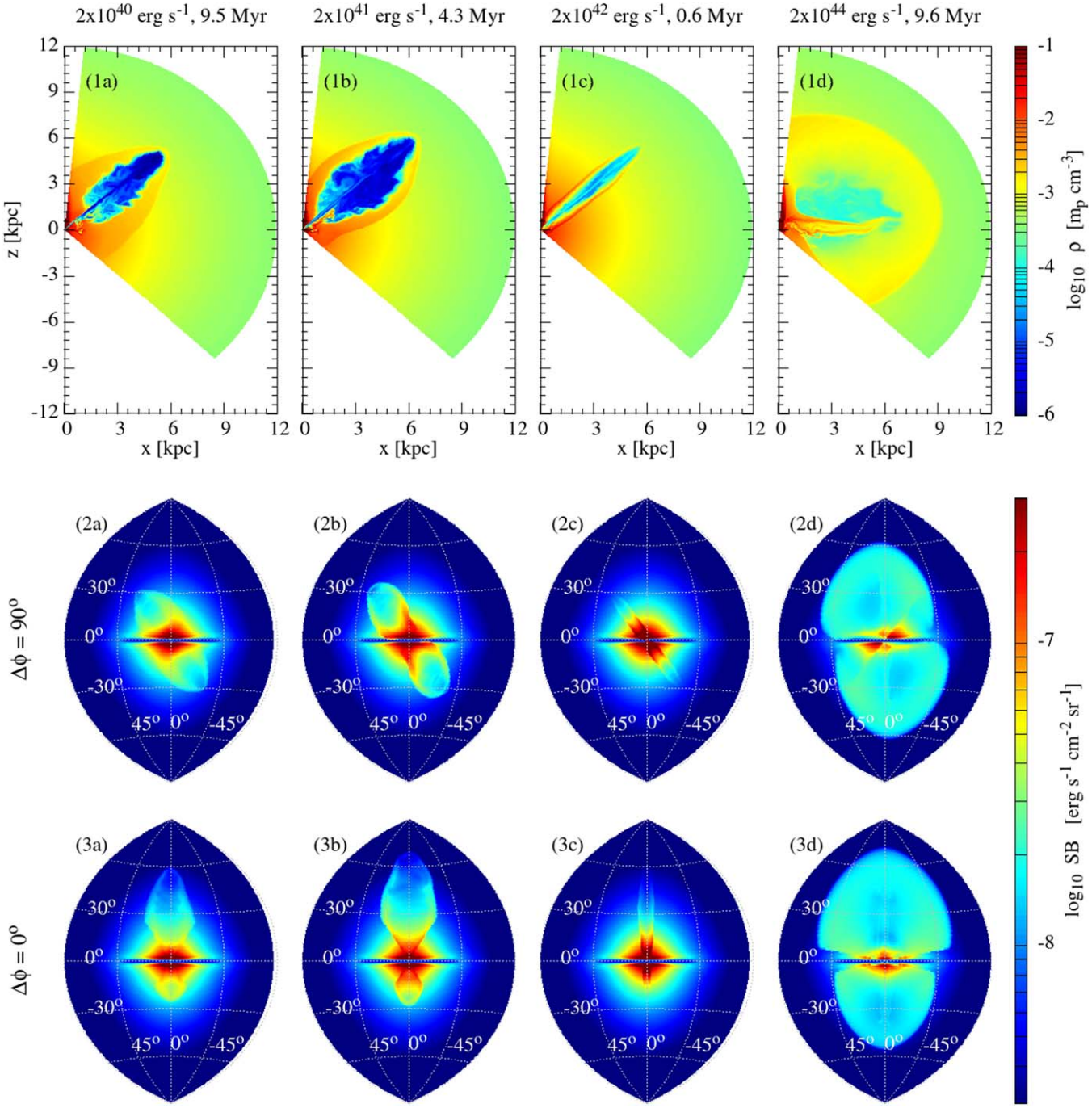

Figure 2. Simulated bubbles for different injected jet powers, $L_j = 2 \times 10^{40}$, 2×10^{41}, 2×10^{42}, and 2×10^{44} erg s^{-1} from left to right, at the GC. The jet is switched off once a total jet energy of 10^{56} erg has been injected. The top panels show the density contours for different jets. The middle and bottom panels correspond to the projected soft X-ray (0.5–2.0 keV) surface brightness maps (assuming MEKAL plasma model) for viewing angles $\Delta\phi = 90°$ (in-plane view) and $\Delta\phi = 0°$ (out-of-plane view), respectively. The snapshots are taken respectively at $t = 9.5$, 4.3, 0.6, and 9.6 Myr. The different timescales reflect the different times it takes to deposit the required energy. For the 2×10^{44} erg s^{-1} case, the long age for the cocoon is due to an early switching off of the jet once the jet reaches the total required energy, $E_{\rm FEBs}$(see discussion around Equation (1) and Section 3.2). The cocoon evolution in this case is different from that of the active jets (see Section 3). The wedge shape at the base of the cocoons is due to the limited range of the simulation box in the ϕ-direction. We increase the ϕ-range of our 2×10^{44} erg s^{-1} case to 10°–170° for a more realistic X-ray map.

the FEBs ($E_{\rm FEBs} = 10^{56}$ erg). Additionally, the cocoon would have been elongated, and it would not have resembled the observed FEBs.

3. Dissipation of the Nuclear Jet

Propagation of jets in an ambient medium and the dynamics of the cocoon are relatively well-studied in the literature (e.g., Begelman & Cioffi 1989; Martí et al. 1997; Matzner 2003; Bromberg et al. 2011). Here, we reproduce some parts of the calculation that are relevant to the current paper. The relativistic jet material interacts with the ambient medium, creating a strong shock in its front. It can be shown (see later) that the shock at the jet head moves much slower than the jet material. The jet material is deflected sideways by the shocked ambient

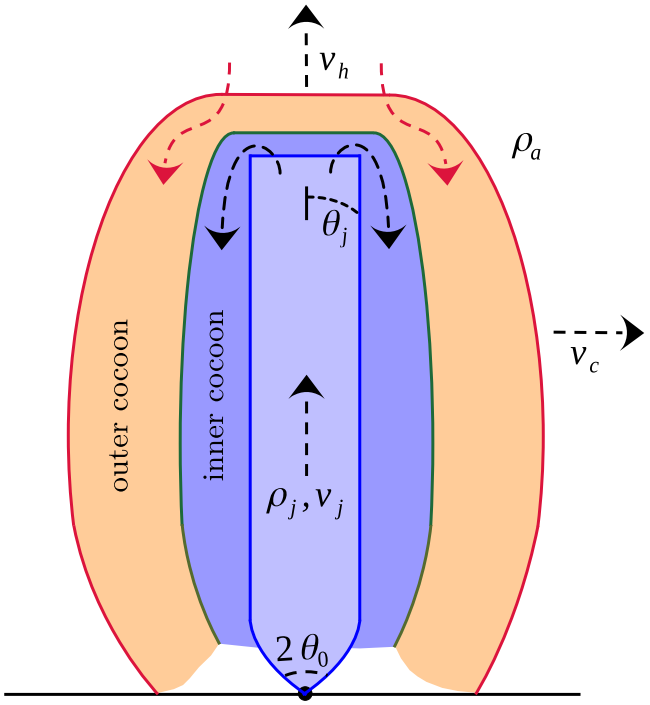

Figure 3. Cartoon of the cocoon geometry. The jet is assumed to be launched with a half opening angle, θ_0, and velocity, v_j. The jet density and half opening angle just before the termination shock are ρ_j and θ_j. The cocoon propagates in an ambient medium with density ρ_a.

material, which creates a reverse shock that converts most of the jet kinetic energy into thermal energy, with a fraction going to turbulent energy. This shocked jet material forms a cocoon (known as the inner cocoon) surrounding the high-velocity jet (see Figure 3). The shocked ambient medium, on the other hand, produces an outer cocoon that forms an outer layer surrounding the inner cocoon. The inner (bluish region in Figure 2) and outer cocoons (orangish region) are separated by a contact discontinuity (the boundary between the bluish and orangish regions) because they have the same pressure.[11]

For a jet with a power L_j, half opening angle θ_j (at the jet head), and a jet velocity v_j, we can write the head velocity of the cocoon as (Martí et al. 1997; Matzner 2003; Bromberg et al. 2011)

$$\beta_h = \beta_j \frac{\Gamma_j\sqrt{\chi}}{1+\Gamma_j\sqrt{\chi}} \approx \beta_j\,\Gamma_j\sqrt{\chi}, \tag{2}$$

where $\beta = v/c$, $\chi = \rho_j/\rho_a$ (for cold jets), and ρ_a is the ambient density (in this case, ISM/CGM). The suffixes h and j represent the head and the jet. The value of χ (jet density contrast relative to the ambient medium) can be obtained by considering that the jet luminosity (including the jet in the opposite direction) is given by

$$\begin{aligned} L_j &= \pi\theta_j^2 z_h^2\ \rho_j\beta_j^3 c^3 \quad \text{(NR)} \\ &= 2\pi\theta_j^2 z_h^2\ \rho_j c^3\ \Gamma_j^2 \quad \text{(ER)}. \end{aligned} \tag{3}$$

[11] The terminology "cocoon" differs between the Blazar and GRB communities. In the Blazar community, the term cocoon only means the inner cocoon, whereas the GRB community refers both to the inner and outer cocoons together as the "cocoon." Here, we follow the GRB community convention.

Here, Γ_j is the Lorentz factor of the jet material and z_h is the height of the jet head. The terms NR and ER denote nonrelativistic and extremely relativistic dynamics, respectively. Therefore, Equation (2) is

$$\begin{aligned} v_h &\approx 300\ \text{km s}^{-1}\left(\frac{L_{42}}{n_a}\right)^{1/2}\frac{\beta_j^{-1/2}}{\theta_{j,10^\circ}\ z_{200pc}} \quad \text{(NR)} \\ &\approx 210\ \text{km s}^{-1}\left(\frac{L_{42}}{n_a}\right)^{1/2}\frac{1}{\theta_{j,10^\circ}\ z_{200\text{pc}}} \quad \text{(ER)}, \end{aligned} \tag{4}$$

where $L_{42} = L_j/(10^{42}\text{erg s}^{-1})$, $n_a = \rho_a/(0.6\,m_p)$, $\theta_{j,10^\circ} = \theta_j/10^\circ$, and $z_{200\text{pc}} = z_h/200$ pc. We note that the apparent discontinuity in the extremely relativistic and nonrelativistic velocities is due to different approximations for the energy in these two regimes, because the NR approximation breaks down at $\beta \gtrsim 0.75$, i.e., $\Gamma \gtrsim 1.5$. This discontinuity in the NR and ER cases propagates to the other equations as well. It is clear that, for typical ISM/CGM conditions, the jet head is nonrelativistic, i.e., $\Gamma_j\sqrt{\chi} \ll 1$, even if the jet material is moving with relativistic velocities (justifying the second equality in Equation (2)).

It should be noted that the half opening angle, θ_j, at the jet head can be very different from the intrinsic jet opening angle, θ_0, at the base of the jet. Bromberg et al. (2011) showed that the jets are always collimated from a conical geometry to a cylindrical geometry in their passage through the ISM if (Equation (30) in their paper)

$$L_j \lesssim 1.5 \times 10^{49}\text{erg s}^{-1} z_{200\text{pc}}^2\ \theta_{j,10^\circ}^{2/3}\ n_a. \tag{5}$$

This is well above the Eddington luminosity of the Sgr A*, and we can expect that typical jets from Sgr A* will be collimated to a cylindrical shape during their passage through the ISM ($n_a \sim 1$, and $z_h \sim 200$ pc). The opening angle for the collimated jet can be written as (using Equations B3 and B9 of Bromberg et al. 2011)

$$\theta_j = 0.^\circ 55\ L_{42}^{1/6}\theta_{0,10^\circ}^{8/15} z_{200\text{pc}}^{-1/3} n_a^{-1/6}, \tag{6}$$

where $\theta_{0,10^\circ} = \theta_0/10^\circ$. The jet-head velocity can now be written as

$$\begin{aligned} \frac{v_h}{\text{km s}^{-1}} &\approx 5500\left(\frac{L_{42}}{n_a}\right)^{1/3} z_{200\text{pc}}^{-2/3}\theta_{0,10^\circ}^{-8/15}\beta_j^{-1/2}\ \text{(NR)} \\ &\approx 3400\left(\frac{L_{42}}{n_a}\right)^{1/3} z_{200\text{pc}}^{-2/3}\theta_{0,10^\circ}^{-8/15}\ \text{(ER)}. \end{aligned} \tag{7}$$

The sideways expansion velocity, v_c, of the cocoon can be estimated from the cocoon pressure, P_c ($=3/4\rho_a v_c^2$). Because the total thermal energy of the cocoon is simply the energy injected by the jet at any given time, $P_c = (\gamma-1)L_j t/(\pi R_c^2 z_h)$, where we assume the cocoon to be a cylinder with radius $R_c \sim v_c t$ and height $z_h \sim v_h t$. This allows us to solve for the cocoon expansion velocity as

$$\begin{aligned} \frac{v_c}{\text{km s}^{-1}} &\approx 1420\left(\frac{L_{42}}{n_a}\right)^{1/3} z_{200\text{pc}}^{-2/3}\theta_{0,10^\circ}^{-2/15}\beta_j^{-1/8}\ \text{(NR)} \\ &\approx 1300\left(\frac{L_{42}}{n_a}\right)^{1/3} z_{200\text{pc}}^{-2/3}\theta_{0,10^\circ}^{-2/15} \quad \text{(ER)}. \end{aligned} \tag{8}$$

As a quick check for the HP case ($L_{42} = 1$), we estimate that $v_h = 12700$ km s^{-1} (simulation) and $=11,800$ km s^{-1} (theory). For the cocoon velocity, we estimate $v_c = 1350$ km s^{-1} (simulation), and $=1280$ km s^{-1} (theory) for an assumed average density $n_a = 2 \times 10^{-3}$ and jet head location $z = 8$ kpc. The simulation and the theory are therefore reasonably consistent. A detailed study of the theory and its comparison to simulations is beyond the scope of this paper, but one is given in Harrison et al. (2018).

3.1. Active Jet

As mentioned, we define jet dissipation as the process in which the jet energy is deposited in a thermal cocoon and the resulting cocoon follows the large-scale density gradient. In this way, the outflow forgets the initial direction of the jet. Qualitatively, it happens when the cocoon produced by the jet expands purely due to its internal pressure rather than the ram pressure.

It can be easily seen from Equations 7 and 8 that $v_h/v_c \approx 3.9\ \theta_{0,10^\circ}^{-2/5}\beta_j^{-3/8}$ for nonrelativistic jets and $\approx 3\ \theta_{0,10^\circ}^{-2/5}$ for relativistic jets. This means that, as long as the jet is active, the cocoon will be always significantly elongated along the jet axis, meaning that the cocoon does not expand purely due to its internal pressure. This is consistent with our simulations of LP, MP, and HP cases that are continuously active (see Figure 2). In the context of the FEBs, we conclude that an active (or more recently switched off) jet in the Galaxy would always maintain its direction and would not produce the observed symmetric FEBs.

3.2. Choked Jet

Dissipation will happen if the jet is switched off (choked) before it breaks out of the ISM. A choked jet will deposit its kinetic energy as thermal energy inside the ISM. The subsequent cocoon evolution is then similar to a blast wave that follows the ambient density gradient and can produce axisymmetric and hemisymmetric features around the Galactic plane. The condition for choking and a subsequent vertical rise of the cocoon is $t_{\rm inj} \lesssim H_{\rm ISM}/v_h$, where $H_{\rm ISM}$ is the height of the ISM ($\sim$200 pc). As the jet duration depends on the jet power (see Equation (1)), there is a critical jet power above which the jet will choke before it can escape from the ISM (using Equation 7):

$$\frac{L_{\rm choke}}{\rm erg\ s^{-1}} \approx 8.6 \times 10^{44} E_{56}^{3/2}\theta_{0,10^\circ}^{-4/5} H_{200\rm pc}^{-5/2} n_a^{-1/2}\beta_j^{-3/4}\ ({\rm NR})$$
$$\approx 5 \times 10^{44} E_{56}^{3/2}\theta_{0,10^\circ}^{-4/5} H_{200\rm pc}^{-5/2} n_a^{-1/2}\ ({\rm ER}), \quad (9)$$

where $H_{200\rm pc} = H_{\rm ISM}/200$ pc. Less powerful jets will escape unchoked. Qualitatively, high-power jets choke because they are switched off early to produce a given total energy.

Figure 4 shows the behavior of $L_{\rm choke}$ with the intrinsic jet opening angle, θ_0. We see that, for reasonable jet opening angles (i.e., $\theta_0 \lesssim 10^\circ$), choking happens at $L_j \gtrsim L_{\rm Edd}$. This limit is in excellent agreement with our simulations as shown in Figure 2. In Section 2, we used geometrical arguments to show that highly inclined jets that have not been choked should produce either axisymmetric or hemisymmetric FEBs, but not both. Thus, to produce an FEB that is both axisymmetric and hemisymmetric, the jet must have been choked at some point. Our analysis in this section shows that for, such a case, the jet luminosity must have been above the Eddington limit ($\approx 5 \times 10^{44}$ erg s^{-1} for MW SMBH) for reasonable values of the jet parameters and the ISM. Such a choked jet is similar to the nonjetted injection in Mondal et al. (2022) or Yang et al. (2022). We also note that our choked jet cases are very similar to the eROSITA-like bubbles seen in Illustris TNG50 simulation suite in the cases where the jets are switched off early (Pillepich et al. 2021). In many cases, Pillepich et al. (2021) also note that the jet inclination is maintained when the jet is still active or was active until very recently.

While the simulations provide us a glimpse of the dissipation processes happening for a given set of jet parameters, Figure 4 shows a comprehensive view of the parameter space. The red shaded region represents where the jet is active for a longer period of time and is not dissipated within the ISM. Although the white region above $L_{\rm choke}$ can, in principle, dissipate jets inside ISM, the required jet has to be super-Eddington for a reasonable value of intrinsic jet opening angle ($\lesssim 10^\circ$). In the next section, we show that such super-Eddington jets are not compatible with the X-ray observations.

4. The O VIII/O VII Ratio

One of the main constraints on the dynamics of the FEBs comes from the observed O VIII/O VII line ratio toward the bubbles (Miller & Bregman 2016). Using hydrodynamical simulations, Sarkar et al. (2017) showed that the observed line ratio is roughly compatible with a power $\approx 10^{40.5-41}$ erg s^{-1} for quasi-spherical flows such as a wind driven by star formation or an accretion wind around Sgr A* that is still active. Now turning to highly powerful jets that are choked ($t_j \lesssim 6$ kyr), the luminosity limit provided by Sarkar et al. (2017) does not apply, because the jets are no longer active. Following Sarkar et al. (2017), we obtain a similar estimate for the O VIII/O VII line ratio for the choked jets below and show that a super-Eddington, short-duration burst is incompatible with the observed line ratio.

Given that the choked jets have super-Eddington power, the events have to be short-lived ($t_{\rm inj} \lesssim E_{\rm FEBs}/L_{\rm Edd} \approx 6$ kyr) to produce the energy of the FEBs. Therefore, we can assume that a choked jet is simply an explosion at the Galactic center and its dynamics can be modeled as a blast wave propagating through the CGM, i.e., $r_s = A(Et^2/\rho)^{1/5}$. Here, $A \sim 1$, $E = 10^{56}$ erg is the energy of the blast, t is the time, and ρ is the ambient density. For a power-law density profile, i.e., $\rho(r) = \rho(r_0)\ (r/r_0)^{-\alpha}$, the above equation can be modified to write down the shock radius and velocity as

$$r_s = A^{5/(5-\alpha)}\left(\frac{E}{\rho_0 r_0^\alpha}\right)^{1/(5-\alpha)} t^{2/(5-\alpha)}$$
$$v_s = \frac{d}{dt}r_s = \frac{2}{5-\alpha}\frac{r_s}{t}. \quad (10)$$

The dynamical time to reach a certain radius R_s therefore is $t_{\rm dyn} = A^{-5/2}R_s^{(5-\alpha)/2}(\rho_0 r_0^\alpha/E)^{1/2}$. For the MW CGM, we assume $\rho_0 = 1.2 \times 10^{-2}\ m_{\rm p}$ cm^{-3}, $r_0 = 1$ kpc, and $\alpha = 1.5$ (Miller & Bregman 2015). We also note that the above blast wave solution is only valid for an ambient medium with negligible pressure, and it needs modifications if the ambient medium has significant pressure (which is the case for the

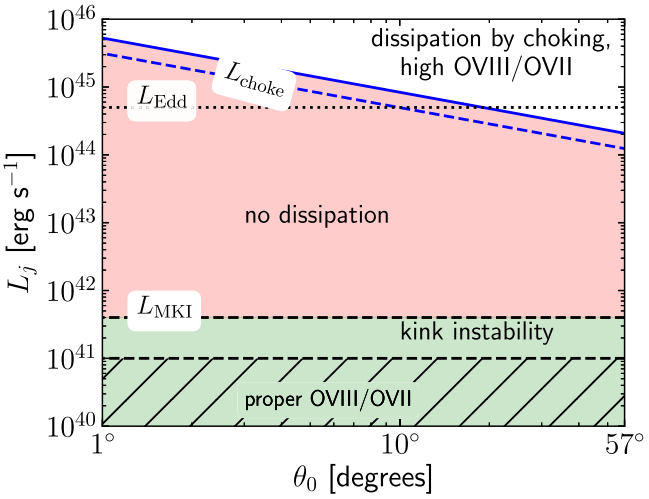

Figure 4. Constraints on the AGN jet luminosity. The red shaded area represents the parameter space for which the jet does not dissipate, and hence it is ruled out. The blue lines represent the luminosity above which the jet is choked and produces a blast wave type cocoon, irrespective of the initial jet direction. For a reasonable intrinsic jet opening angle (i.e., $\theta_0 \lesssim 10°$), the jet requires Eddington/super-Eddington luminosity to be choked (because $t_{inj} = E_{FEBs}/L_j$). The blue solid and dashed lines represent the nonrelativistic and relativistic limits, respectively. The x-axis extends until $\theta_0 = 1$ radian (57^0) because relativistic jets are no longer causally connected above $\theta_0 \gtrsim 1/\Gamma_j$ and behave as a spherical wind. The green region shows where a magnetically dominated jet can be dissipated via kink instability. The hatched region shows the limit where O VIII/O VII line ratio is consistent with observations (Sarkar et al. 2017). We note that the analytical solution becomes increasingly invalid beyond $\theta_0 \gtrsim 10°$, as the analytical considerations are only for a small jet opening angle.

CGM). To quantify this, we have run an idealized hydrodynamical simulation of a blast wave in the above power-law density profile using PLUTO (Mignone et al. 2007). We calibrate the value of A against the simulated shock and find that $A = 1.02$ describes the shock well for our purposes here. Therefore, the dynamical time is

$$t_{dyn} \approx 12\mathrm{Myr} R_{s,10}^{7/4} E_{56}^{-1/2}, \quad (11)$$

where $E_{56} = E_{FEBs}/10^{56}$ erg.

For strong shocks, it is often the case that the electron temperature, T_e, is not the same as the proton temperature, T_p, or the shock temperature, T_{eq}. Such deviation from nonequilibrium arises due to a long Coulomb interaction timescale (Spitzer 1956),

$$t_{eq} \sim 2\mathrm{Myr}\left(\frac{T_e}{4\times10^6\,\mathrm{K}}\right)^{3/2}\left(\frac{10^{-3}}{n_a}\right) \sim 3.3\mathrm{Myr}\left(\frac{T_e}{4\times10^6\,\mathrm{K}}\right)^{3/2} R_{s,10}^{3/2}, \quad (12)$$

compared to the dynamical timescale, t_{dyn}, of the shock. Here, $R_{s,10} = R_s/10$ kpc and we have used the CGM density profile as mentioned earlier. In such cases, one needs to solve for the electron temperature before comparing it with the observations. However, we find that (see Appendix C and the left panel of Figure 5) the e-p interaction timescale for the blast wave, even assuming just Coulomb coupling, is short enough (due to a low Mach number of the shock) that the electrons and protons are in equilibrium. Therefore, the shock temperature of the blast wave is a good indicator of the electron temperature for such a blast wave, in contrast to the assumption of $T_e \ll T_p$ needed for the Yang et al. (2022) parameters to match the observed O VIII/O VII line ratio.[12]

The middle panel in Figure 5 shows the O VIII/O VII line intensity ratio corresponding to the electron temperature at a given radius. The line ratios for given electron temperatures are obtained from CLOUDY-13.04 (Ferland et al. 2013). The blue line represents the line ratio if the electron temperature is solved until $t = t_{dyn}(R_s)$, starting from the post-shock values at that time, while the orange line simply assumes instantaneous equilibrium. The blue shaded region represents the observed values (Miller & Bregman 2016). The figure shows that T_e and T_p are in equilibrium at $r \gtrsim 2$ kpc and that at $R_s = 10$ kpc (roughly the size of the FEBs), the expected O VIII/O VII ratio is much higher than the observed range of values. We also confirm this by calculating the projected intensity ratio map of O VIII/O VII for the EP case (similar to Figure 5 in Sarkar et al. 2017). For a realistic ratio map, we also consider the effect of the extended CGM until 100 kpc. We show the histogram of the line ratio in the projected map in the right panel of Figure 5 and compare it with the observations (Miller & Bregman 2016). Clearly, such high-energy blast waves are not consistent with the observed O VIII/O VII and hence do not describe the FEBs.

5. Discussion

5.1. Magnetic Kink Instability

An aspect that we have not discussed so far is the possibility of the magnetic kink instability (MKI; Bromberg & Tchekhovskoy 2016; Tchekhovskoy & Bromberg 2016). MKI appears in magnetically dominated jets. It destabilizes the smooth flow of the jet by enhancing instabilities at the jet–cocoon boundary. The timescale to grow MKI is typically ~10 Alfvén crossing times across the jet width. This indicates a critical jet length after which the laminar jet flow turns into a turbulent one, thus causing jet dissipation. The critical luminosity below which the jet dissipates within a given length scale of the ambient medium (in this case, the ISM) can be written as (Eq. 2 of Bromberg & Tchekhovskoy 2016; Tchekhovskoy & Bromberg 2016)

$$L_{MKI} = 4\times10^{41}\mathrm{erg\ s^{-1}} n_a H_{200pc}^2 \quad (13)$$

for a flat density profile until height H_{200pc}. This limit has been shown using the black dashed line in Figure 4. This upper limit of the jet luminosity is slightly higher than, but consistent with, the observed O VIII/O VII line ratio (Miller & Bregman 2016; Sarkar et al. 2017; shown by the black hatched region in Figure 4). Thus, a magnetically dominated jet with power $\approx 10^{40.5-41}$ erg s^{-1} can produce the symmetric FEBs that are also consistent with the X-ray observations.

5.2. Accretion Disk Wind

Wind from the accretion disk around the central black hole is another process that can launch a wide-angle (~30°) ultra-fast outflow that couples to the ambient medium much more than the jets (King & Pounds 2003; Hopkins & Elvis 2010;

[12] We also solve for the electron temperature for a blast wave with an energy $E = 10^{57}$ erg (as assumed in Yang et al. 2022). We find that, although T_e lags behind T_p at $t = t_{dyn}$ due to the Coulomb timescale, in this case, $T_e(t = t_{dyn}) \approx 8\times10^6$ K. This temperature is much larger than the required value of $\approx 3\times10^6$ K for explaining the O VIII/O VII line ratio.

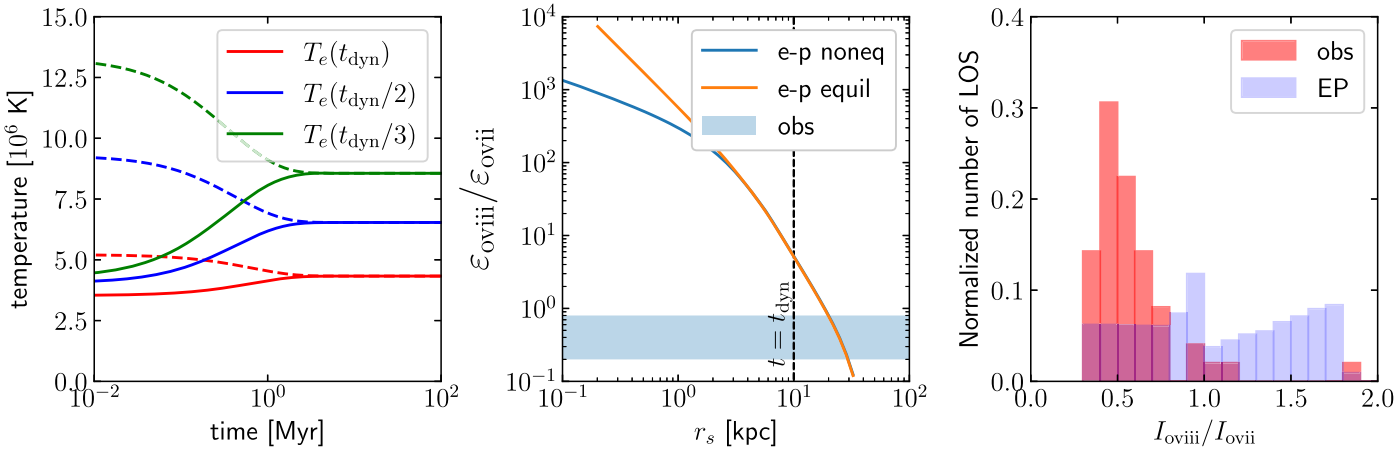

Figure 5. Left: Evolution of electron (T_e; solid lines) and proton (T_p; dashed lines) temperatures in the post-shocked gas that is shocked at different times ($t_{\rm dyn}$, $t_{\rm dyn}/2$, and $t_{\rm dyn}/3$). Here, $t_{\rm dyn}$ represents the time for the blast wave to reach $R_s = 10$ kpc, and the time is measured after this instant. $T_e - T_p$ equilibrium happens almost instantaneously for shocks that are $\gg$1 Myr old. Middle: O VIII/O VII emissivity ratio corresponding to the electron temperature behind the shock at different stages of its evolution. The orange line shows the ratio if we assume that the $T_e = T_{\rm eq}$, and the blue line shows the values if e-p temperature nonequilibrium is assumed. The blue shaded region shows the observed ratio, and the black vertical line shows the expected ratio at $R_s = 10$ kpc. Right: histogram of the line ratio in the projected map (for the EP case) and vs. observations (Miller & Bregman 2016). Ratio values <0.3 are intentionally removed to avoid the background CGM contribution.

King 2010; Faucher-Giguère & Quataert 2012; Wagner et al. 2013; Jiang et al. 2019). Such quasi-spherical winds from Sgr A* can be another source of energy that can inflate the FEBs and produce the symmetrical features of the FEBs (Yuan et al. 2012; Mou et al. 2014, 2015). Sarkar et al. (2017) showed that the wide-angle winds follow the observed O VIII/O VII line ratio only if the wind power is $10^{40.5-41}$ erg s^{-1} ($\sim 10^{-4}$ $L_{\rm Edd}$). Such a wind should sustain for $\sim$30 Myr (to produce 10^{56} erg energy). However, in such a low-luminosity AGN (LLAGN) the feedback is mostly dominated by jets rather than by winds (Yuan et al. 2012; Yuan & Narayan 2014; Giustini & Proga 2019). The jet, on the other hand, would fail to produce the symmetrical features of the FEBs (see Section 3) unless it is magnetized and has low energy. Therefore, the role of accretion wind as the source of FEBs' energy remains uncertain.

5.3. Tidal Disruption Events

An interesting possibility, that will be explored further elsewhere (T. Piran et al. 2023, in preparation), is that outflow from Tidal Disruption Events (TDEs) at the central black hole is a major or even dominant source of energy powering the FEBs. The nuclear star cluster feeds the central black hole with stars leading to TDEs. A TDE results in an unbound material and possibly in an outflow powered by the accretion onto the black hole and at times in jets. As the stars are fed in different orientations, the outflows will be directed in different directions. This results in an overall quasi-spherical wind that resembles the outcome of SNe or accretion-driven winds discussed earlier.

It is estimated that an MW-type black hole (mass 4×10^6 $M_\odot$) has a typical TDE rate of $\sim 10^{-4}$ yr^{-1} (Stone & Metzger 2016). The total energy produced from such events at the central black hole is debated. Typically, 3×10^{51} ergs are ejected as the unbound material (Piran et al. 2015). This energy is insufficient to power the FEBs, as it would result only in an average luminosity of $\sim 3 \times 10^{51}$ erg $\times 10^{-4}$ yr$^{-1} \approx 10^{40}$ erg s^{-1}. If the accreted stellar mass were converted efficiently to radiation by the SMBH, the total energy per TDEs would reach 10^{53} erg, which would be sufficient to power the FEBs (Ko et al. 2020). However, it is currently debatable whether the total energy output of TDEs is so high (see, e.g., Svirski et al. 2017). Alternatively, an enhanced rate of TDEs at the GC (T. Piran et al. 2023, in preparation) could explain the observations.

5.4. Star Formation Driven Wind

Supernovae (SN) explosions from the ongoing star formation at the Galactic center could be another possible source of energy for the FEBs (Sarkar et al. 2015b; Crocker et al. 2015). Because the SNe energy is not directional, dissipation of the energy in the ISM happens naturally. The required star formation rate to produce the FEBs is $\approx$0.3–0.5 $M_\odot$ yr^{-1} over a timescale of last $\approx$30 Myr (Sarkar et al. 2015b). This required rate and its duration are well within the observed star formation rate of 0.2–0.8 $M_\odot$ yr^{-1} (within the central $\sim$50 pc) over the last $\sim$30 Myr (Nogueras-Lara et al. 2020).

6. Conclusions

We have run 3D hydrodynamical simulations of jets at the Galactic center that are significantly tilted from the Galaxy rotation axis. The tilted jets are inspired by the observations of subpc gaseous/stellar streams and the recent EHT results of the accretion disk around the MW SMBH (Genzel et al. 2010; Akiyama et al. 2022). Using the simulations and analytical considerations, we show that:

1. Jet dissipation inside the ISM is a necessary condition to produce the observed axisymmetric (symmetry around rotation axis) and hemisymmetric (symmetry around Galactic plane) Fermi/eROSITA bubbles (FEBs).
2. Jet dissipation does not happen for nonmagnetic jets with power $L_j \lesssim L_{\rm Edd}$. Jets with higher power dissipate their energy into the ISM via early choking ($t_{\rm inj} \lesssim 6$ kyr) before they break out of the ISM. Such Eddington power jets, however, produce overly high O VIII/O VII line ratios compared to the observations (even after considering electron–proton temperature nonequilibrium) and are ruled out.

Therefore, we arrive at the conclusion that nonmagnetic jets from the Sgr A* do not reproduce the morphology as well the

X-ray constraints of the FEBs. We speculate that the excess ionization observed in the direction of the Magellanic streams (Bland-Hawthorn et al. 2019) might be due to a more recent AGN event (∼a few Myr ago) that also produced the subpc stellar structures and the ∼100 pc radio bubbles in Sgr A* (Ponti et al. 2019) but did not produce the FEBs. It is possible that the above ∼Myr jet event is one of many such events that powered the FEBs, but it may not necessarily be the case.

Based on the necessity of jet dissipation as presented in this paper, we can limit the remaining options for the origin of the FEBs as follows.

1. *Star Formation Driven*: Wind driven by supernovae from the star-forming region at the Galactic center naturally produces symmetric cocoons because supernovae explosions do not have any preferred direction (see Sarkar et al. 2015a, 2017; Sarkar 2019). The required star formation rate ($\sim 0.5\ M_{\odot}\mathrm{yr}^{-1}$) in these models is within the observational limits (Nogueras-Lara et al. 2020).
2. *Weak Magnetic Jets or Accretion Winds*: If nuclear jets are indeed magnetically dominated, then jet dissipation by kink instability is a possibility. Winds from the past accretion disk naturally satisfy the condition for dissipation. The required magnetic-jet/accretion wind power (i.e., $\approx 10^{40.5-41}$ erg s^{-1}; Mou et al. 2014, 2015) is consistent with the O VIII/O VII line ratio as well as the enhanced past accretion rate in Sgr A* (Totani 2006).
3. *Tidal Disruption Driven*: Wind driven by a succession of tidal disruption events taking place at the Galactic center could satisfy the required energy conditions, provided that the energy per TDE is 10^{52-53} erg (Ko et al. 2020). Alternatively, the required power is also achievable if there was a period of ∼10 Myr during which the Galactic TDE rate was slightly higher than expected, i.e., an event per 10^3 yr (in comparison to the current 10^{-4} yr^{-1}). With energy injection of a few $\times 10^{51}$ erg per event, such an enhanced period of TDEs can supply the needed energy budget (T. Piran et al. 2023, in preparation). This is, however, a future area of research.

In all the above cases, irrespective of star formation or AGN origin, we find that the jet/wind power has to be $\lesssim 10^{41}$ erg s^{-1} to produce symmetric FEBs and satisfy the O VIII/O VII constraint. With such low power, the age of the Fermi Bubbles is estimated to be $\sim 10^{56}$ erg $/(10^{41}\mathrm{erg\ s}^{-1}) \approx 30$ Myr. While a combined AGN and star formation driven scenario looks like an attractive solution for the FEBs, we must note that the presence of one source can suppress the presence of the other (Anglés-Alcázar et al. 2021). It is, therefore, more likely that either the star formation or the AGN-driven wind/jet scenario (with limited power) is more natural.

Acknowledgments

We thank Omar Bromberg, Karamveer Kaur, Dipanjan Mukherjee, Matteo Pais, and Nicholas Stone for helpful discussions. We also thank the anonymous referee for critical comments that improved the quality of the paper. K.C.S. acknowledges support from the German Science Foundation via DFG/DIP grant STE 1869/2-1 GE 625/17-1 and Israeli Science Foundation (ISF) via grant No. 2190/20. S.M. acknowledges a Ramanujan Fellowship (No RJF/2020/000113) provided by SERB-DST, Govt. of India. S.M. also acknowledges the use of the computing resources made available by the Computer Centre (NOVA Cluster) of the Indian Institute of Astrophysics for this work. Some simulations were carried out on the PARAM Pravega cluster at IISc, for which P.S. acknowledges a National Supercomputing Mission (NSM) grant from the Department of Science and Technology, India. P.S. also acknowledges a Swarnajayanti Fellowship (DST/SJF/PSA-03/2016-17). T.P. acknowledges support from Advanced ERC grants TReX and Multijets.

Appendix A
Grid Structure in Our Simulations

The grid structure in our spherical simulations is shown in Figure 6 along different directions. We resolve the central 200 pc with a resolution $\Delta < 2$ pc. The jet base ($r = 30$ pc) is resolved with $\Delta = 0.2$ pc, suitable for properly resolving the jet collimation. We ran a simulation in spherical coordinates with twice the spatial resolution for the MP case ($L_j = 2 \times 10^{41}$

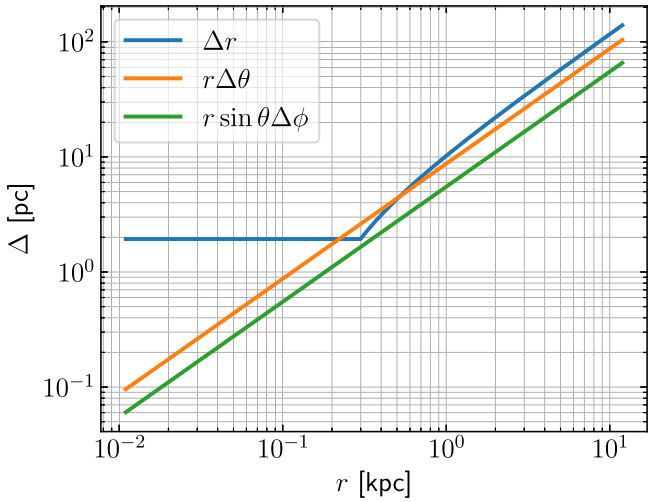

Figure 6. Resolutions in the r, θ, and ϕ directions (here, $\theta = 45°$) in our spherical grid simulations. The respective resolutions are $\Delta < 2$ pc at $r < 200$ pc (in the ISM) and $\Delta \sim 0.2$ pc at $r = 30$ pc (at the jet base).

erg s^{-1}) and found that the currently adopted resolution is suitable to produce a converged shape of the cocoons.

Appendix B
Comparing with Previous Simulations

In addition to the simulations in the spherical coordinates, we also perform simulations in 3D Cartesian coordinates. In this setup, the simulation box extends from −9 to +9 kpc in the *X*- and *Y*-directions, and from −11 to +11 kpc in the Z-direction. The ISM disk is set to lie on the *X*–*Y* plane. To understand the effects of resolution and compare them with those in other works, we run our MP case ($L_j = 2 \times 10^{41}$ erg s^{-1}) at two resolutions. For the low-resolution case, we use $\Delta_{\rm ISM} = 4$ pc resolution in the central ±200 pc in all the directions and $\Delta_{\rm CGM} = 50$ pc in the rest of the simulation box. In the high-resolution simulation, we increase the overall resolution by a factor of two throughout the box. The jet was injected at an angle of 45° from the Galaxy rotation axis and in a region within a half opening angle of 5° and $r \leqslant 30$ pc in the same fashion as in the main simulations (Section 2.1).

Figure 7 shows the results for the two simulations. The velocity maps show that the jet widens as soon as it leaves the jet injection region. The widening is worse in the case of the lower-resolution simulation. The higher-resolution simulation does a slightly better job at resolving the collimated structures at the jet base. The significant difference between the two runs suggests that much finer grid spacing is needed (for a Cartesian grid) to resolve the jet and in particular its collimation, which in turn determines its overall fate. The spherical coordinate system, on the other hand, naturally resolves the central base of the jet (see Figure 6).

Several simulations of jet–ISM interaction show dissipation of the jets in the ISM (such as Mukherjee et al. 2018; Tanner & Weaver 2022). These simulations employ Cartesian coordinates with a resolution of ∼5–10 pc to resolve the jet with a base ∼30 pc wide. As we see in Figure 7, comparable simulations with grid spacings of 2 pc and 4 pc did not converge, with the higher-resolution run showing more collimation. Based on these simulations, we speculate that the dissipation seen in the earlier jet–ISM simulations could be partially due to an insufficient spatial resolution.

There could be other reasons for the difference between our results and the results of previous simulations. The ISM itself was assumed to be extended until ∼0.5–1 kpc and significantly

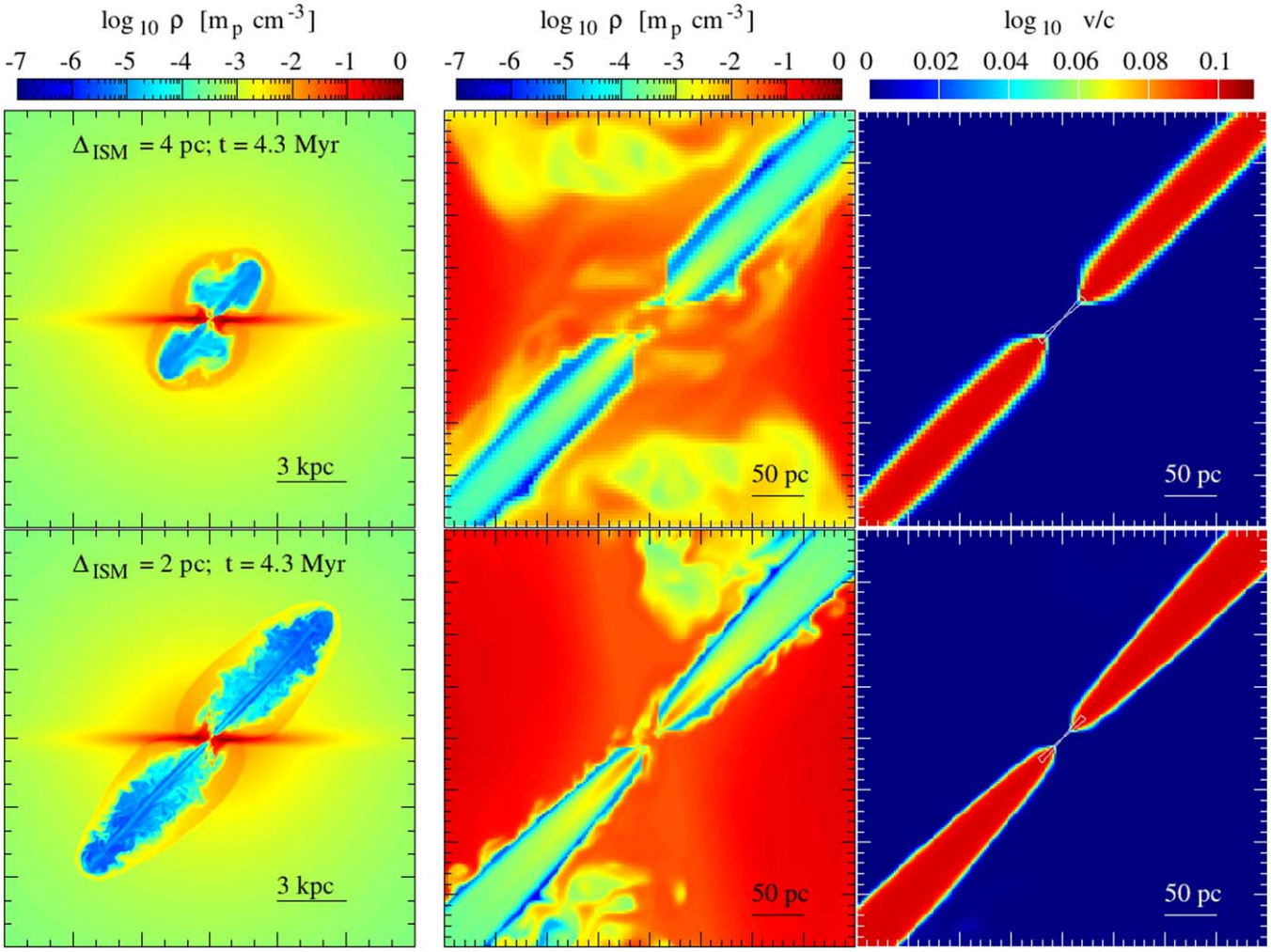

Figure 7. Comparing two resolutions for $L = 2 \times 10^{41}$ erg s^{-1} simulations. The simulations are run in Cartesian coordinates and the plots show an $X - Z$ slice at $y = \Delta/2$. The top panel shows results from the low-resolution run ($\Delta_{\rm ISM} = 4$ pc) and the bottom panel shows the results from the higher-resolution run ($\Delta_{\rm ISM} = 2$ pc) at the same time, i.e., $t = 4.3$ Myr. The first column shows the density map for the entire box, the second column shows a zoomed-in version of the density within the central ±100 pc, and the third column shows the zoomed-in velocity maps. The higher-resolution jets are less dissipated, owing to lower jet surface area and a sharper jet–ISM boundary. The white cones represent the intended region of jet injection.

clumpy (volume-filling factor ∼0.2–0.5), with clump sizes as large as ∼300 pc. However, the volume-filling fraction for the clumpy ISM gas, $\sim 10^{-3}$ (Draine 2011), is much lower in the Milky Way.

Appendix C
e-p Nonequilibrium

We solve for T_e and T_p considering only Coulomb interaction between electrons and protons (Braginskii 1965), i.e.,

$$\frac{3}{2} n_e \frac{dT_e}{dt} = -3 \frac{m_e}{m_p} \frac{n}{\tau_e} (T_e - T_i)$$
$$\frac{3}{2} n_i \frac{dT_i}{dt} = 3 \frac{m_e}{m_p} \frac{n}{\tau_e} (T_e - T_i), \quad \text{(C1)}$$

where $\tau_e = 3.44 \times 10^{5} \frac{(k_B T_e / \mathrm{eV})^{3/2}}{n\lambda}$, $\lambda \approx 15$, and $n = \rho/(0.6\, m_p)$ is the particle number density, $n_e = \rho/(1.15\, m_p)$ is the electron number density, and $n_i = \rho/(1.27\, m_p)$ is the ion number density for a fully ionized plasma. These equations can be solved for a given set of initial conditions. The initial values for T_e and T_p are assumed to be the temperatures in a post-shocked gas and are calculated following Vink et al. (2015; their Equations 19 and 21, which are based on adiabatic heating and thermalization of electrons at shocks and match observations of collisionless shocks) for a given Mach number of the shock. The evolution of the temperatures has been shown in the left panel of Figure 5. Different colors show different starting values for the post-shock gas ($t_{\rm dyn}$ is the dynamical time for $r_s = 10$ kpc). The figure shows that, at early times ($t = t_{\rm dyn}/3 \approx 4$ Myr) of the blast wave, the starting $T_e/T_p \approx 0.3$. The temperatures, however, quickly become equal within ∼1 Myr. Incidentally, the equilibrium timescale at any stage of the shock is about the same, for the given density profile. This implies that, for older shocks (age ≫1 Myr), the electrons and protons will have enough time to be in equilibrium. Given that the dynamical time of the FEBs is ∼12 Myr for the EP model, we expect $T_e = T_p = T_{\rm eq}$ in FEBs.

ORCID iDs

Kartick C. Sarkar https://orcid.org/0000-0002-7767-8472
Santanu Mondal https://orcid.org/0000-0003-0793-6066
Prateek Sharma https://orcid.org/0000-0003-2635-4643
Tsvi Piran https://orcid.org/0000-0002-7964-5420

References

Ackermann, M., Albert, A., Atwood, W. B., et al. 2014, ApJ, 793, 64
Agol, E. 2000, ApJL, 538, L121
Akiyama, K., Alberdi, A., Alef, W., et al. 2022, ApJL, 930, L16
Anglés-Alcázar, D., Quataert, E., Hopkins, P. F., et al. 2021, ApJ, 917, 53
Bartko, H., Martins, F., Fritz, T. K., et al. 2009, ApJ, 697, 1741
Begelman, M. C., & Cioffi, D. F. 1989, ApJL, 345, L21
Bland-Hawthorn, J., Maloney, P. R., Sutherland, R., et al. 2019, ApJ, 886, 45
Braginskii, S. I. 1965, RvPP, 1, 205
Bromberg, O., Nakar, E., Piran, T., & Sari, R. 2011, ApJ, 740, 100
Bromberg, O., & Tchekhovskoy, A. 2016, MNRAS, 456, 1739
Cecil, G., Wagner, A. Y., Bland-Hawthorn, J., Bicknell, G. V., & Mukherjee, D. 2021, ApJ, 922, 254
Crocker, R. M., Bicknell, G. V., Taylor, A. M., & Carretti, E. 2015, ApJ, 808, 107
Draine, B. T. 2011, Physics of the Interstellar and Intergalactic Medium (Princeton, NJ: Princeton Univ. Press)
Faucher-Giguère, C.-A., & Quataert, E. 2012, MNRAS, 425, 605
Ferland, G. J., Porter, R. L., van Hoof, P. A. M., et al. 2013, RMxAA, 49, 137
Genzel, R., Eisenhauer, F., & Gillessen, S. 2010, RvMP, 82, 3121
Giustini, M., & Proga, D. 2019, A&A, 630, A94
Guo, F., & Mathews, W. G. 2012, ApJ, 756, 181
Harrison, R., Gottlieb, O., & Nakar, E. 2018, MNRAS, 477, 2128
Hopkins, P. F., & Elvis, M. 2010, MNRAS, 401, 7
Jiang, Y.-F., Stone, J. M., & Davis, S. W. 2019, ApJ, 880, 67
Keshet, U., & Gurwich, I. 2017, ApJ, 840, 7
King, A. R. 2010, MNRAS, 402, 1516
King, A. R., & Pounds, K. A. 2003, MNRAS, 345, 657
Ko, C. M., Breitschwerdt, D., Chernyshov, D. O., et al. 2020, ApJ, 904, 46
Lacki, B. C. 2014, MNRAS, 444, L39
Li, Z., Morris, M. R., & Baganoff, F. K. 2013, ApJ, 779, 154
Liedahl, D. A., Osterheld, A. L., & Goldstein, W. H. 1995, ApJL, 438, L115
Marrone, D. P., Moran, J. M., Zhao, J.-H., & Rao, R. 2006, ApJ, 640, 308
Martí, J. M., Müller, E., Font, J. A., Ibáñez, J. M. Z., & Marquina, A. 1997, ApJ, 479, 151
Matzner, C. D. 2003, MNRAS, 345, 575
Mewe, R., Gronenschild, E. H. B. M., & van den Oord, G. H. J. 1985, A&AS, 62, 197
Mewe, R., Lemen, J. R., & van den Oord, G. H. J. 1986, A&AS, 65, 511
Mignone, A., Bodo, G., Massaglia, S., et al. 2007, ApJS, 170, 228
Miller, M. J., & Bregman, J. N. 2015, ApJ, 800, 14
Miller, M. J., & Bregman, J. N. 2016, ApJ, 829, 9
Mondal, S., Keshet, U., Sarkar, K. C., & Gurwich, I. 2022, MNRAS, 514, 2581
Mou, G., Yuan, F., Bu, D., Sun, M., & Su, M. 2014, ApJ, 790, 109
Mou, G., Yuan, F., Gan, Z., & Sun, M. 2015, ApJ, 811, 37
Mukherjee, D., Bicknell, G. V., Sutherland, R., & Wagner, A. 2016, MNRAS, 461, 967
Mukherjee, D., Bicknell, G. V., Wagner, A. Y., Sutherland, R. S., & Silk, J. 2018, MNRAS, 479, 5544
Mukherjee, D., Bodo, G., Mignone, A., Rossi, P., & Vaidya, B. 2020, MNRAS, 499, 681
Nogueras-Lara, F., Schödel, R., Gallego-Calvente, A. T., et al. 2020, NatAs, 4, 377
Pais, M., Piran, T., & Nakar, E. 2023, MNRAS, 519, 1941
Paumard, T., Genzel, R., Martins, F., et al. 2006, ApJ, 643, 1011
Pillepich, A., Nelson, D., Truong, N., et al. 2021, MNRAS, 508, 4667
Piran, T., Svirski, G., Krolik, J., Cheng, R. M., & Shiokawa, H. 2015, ApJ, 806, 164
Ponti, G., Hofmann, F., Churazov, E., et al. 2019, Natur, 567, 347
Predehl, P., Sunyaev, R. A., Becker, W., et al. 2020, Natur, 588, 227
Rosen, A., Hughes, P. A., Duncan, G. C., & Hardee, P. E. 1999, ApJ, 516, 729
Sarkar, K. C. 2019, MNRAS, 482, 4813
Sarkar, K. C., Nath, B. B., & Sharma, P. 2015a, MNRAS, 453, 3827
Sarkar, K. C., Nath, B. B., Sharma, P., & Shchekinov, Y. 2015b, MNRAS, 448, 328
Sarkar, K. C., Nath, B. B., & Sharma, P. 2017, MNRAS, 467, 3544
Selig, M., Vacca, V., Oppermann, N., & Enßlin, T. A. 2015, A&A, 581, A126
Snyder, J. P. 1993, Flattening the Earth: Two Thousand Years of Map Projections (Chicago, IL: Univ. Chicago Press)
Spitzer, L. 1956, Physics of Fully Ionized Gases, Interscience tracts on physics and astronomy (New York: Interscience) https://books.google.co.il/books?id=uWYFAAAAMAAJ
Stone, N. C., & Metzger, B. D. 2016, MNRAS, 455, 859
Su, M., Slatyer, T. R., & Finkbeiner, D. P. 2010, ApJ, 724, 1044
Svirski, G., Piran, T., & Krolik, J. 2017, MNRAS, 467, 1426
Tanner, R., & Weaver, K. A. 2022, AJ, 163, 134
Tchekhovskoy, A., & Bromberg, O. 2016, MNRAS, 461, L46
Totani, T. 2006, PASJ, 58, 965
Tsuboi, M., Kitamura, Y., Uehara, K., et al. 2018, PASJ, 70, 85
Vink, J., Broersen, S., Bykov, A., & Gabici, S. 2015, A&A, 579, A13
Wagner, A. Y., Umemura, M., & Bicknell, G. V. 2013, ApJL, 763, L18
Yang, H. Y. K., Ruszkowski, M., & Zweibel, E. G. 2022, NatAs, 6, 584
Yuan, F., Bu, D., & Wu, M. 2012, ApJ, 761, 130
Yuan, F., & Narayan, R. 2014, ARA&A, 52, 529
Yusef-Zadeh, F., Royster, M., Wardle, M., et al. 2020, MNRAS, 499, 3909
Zhang, R., & Guo, F. 2020, ApJ, 894, 117
Zhao, J.-H., Morris, M. R., Goss, W. M., & An, T. 2009, ApJ, 699, 186
Zubovas, K., & Nayakshin, S. 2012, MNRAS, 424, 666